

Contents lists available at [SciVerse ScienceDirect](http://SciVerse.Sciencedirect.com)

Computers & Geosciences

journal homepage: www.elsevier.com/locate/cageo

Solid modeling techniques to build 3D finite element models of volcanic systems: An example from the Rabaul Caldera system, Papua New Guinea

Erika Ronchin^{a,b,*}, Timothy Masterlark^b, Joan Martí Molist^a, Steve Saunders^c, Wei Tao^d

^a Grupo de Volcanología de Barcelona (GVB-CSIC), SIMGEO (UB-CSIC), Institute of Earth Sciences Jaume Almera (CSIC), Lluís Solé Sabarís s/n, Barcelona 08028, Spain

^b Department of Geological Sciences, The University of Alabama, Tuscaloosa, Alabama 35487, USA

^c Rabaul Volcano Observatory, P.O. Box 386, Rabaul, East New Britain Province, Papua New Guinea

^d State Key Laboratory of Earthquake Dynamics, Institute of Geology, China Earthquake Administration, Beijing 100029, China

ARTICLE INFO

Article history:

Received 17 May 2012

Received in revised form

19 September 2012

Accepted 20 September 2012

Available online 3 October 2012

Keywords:

Finite Elements Models

3D geometry

Rabaul Caldera

Deformation

ABSTRACT

Simulating the deformation of active volcanoes is challenging due to inherent mechanical complexities associated with heterogeneous distributions of rheologic properties and irregular geometries associated with the topography and bathymetry. From geologic and tomographic studies we know that geologic bodies naturally have complex 3D shapes. Finite element models (FEMs) are capable of simulating the pressurization of magma intrusions into mechanical domains with arbitrary geometric and geologic complexity. We construct FEMs comprising pressurization (due to magma intrusion) within an assemblage of 3D parts having common mechanical properties for Rabaul Caldera, Papua New Guinea. We use information of material properties distributed on discrete points mainly deduced from topography, geology, seismicity, and tomography of Rabaul Caldera to first create contours of each part and successively to generate each 3D part shape by lofting the volume through the contours. The implementation of Abaqus CAE with Python scripts allows for automated execution of hundreds of commands necessary for the construction of the parts having substantial geometric complexity. The lofted solids are then assembled to form the composite model of Rabaul Caldera, having a geometrically complex loading configuration and distribution of rheologic properties. Comparison between predicted and observed deformation led us to identify multiple deformation sources (0.74 MPa change in pressure in the magma chamber and 0.17 m slip along the ring fault) responsible for the displacements measured at Matupit Island between August 1992 and August 1993.

© 2012 Elsevier Ltd. All rights reserved.

1. Introduction

Advancements in computer resources and computational techniques have opened the possibility to apply 3D solid modeling and simulation to large-scale deformation of geological structures. Since the beginning of the application of finite element models (FEMs) to volcanic studies, axisymmetric and two-dimensional models were extensively used (Bianchi et al., 1984; Dieterich and Decker, 1975; Yang et al., 1988). Owing to computational limitations, the early FEM studies predominantly used two-dimensional or axisymmetric modeling, which simulates a magma chamber as a regular shaped fluid-filled cavity. Consequently, these early models lacked geometric fidelity to a natural volcanic system. In fact, model symmetry poorly reflects the highly heterogeneous distribution of properties of

volcanic areas, as well as their topography and bathymetry. As increased computational power became more widely available, larger 3D models became feasible and results from three-dimensional models were increasingly reported in the literature (Currenti et al., 2011a; Masterlark et al., 2012; Meo et al., 2007; Trasatti et al., 2008). Up to now, most approaches for 2D and 3D modeling of volcano crustal deformation and stress distributions have been based on applications of pressure loads, embedded in either homogeneous or layered elastic half-spaces (Dieterich and Decker, 1975; Geyer and Gottsmann, 2010; Gudmundsson and Brenner, 2004; Gottsmann et al., 2006; Pritchard and Simons, 2004; Trasatti et al., 2003).

Due to the complex history and array of physical and chemical processes occurring in volcanic areas, volcanic systems are characterized by abrupt spatial variations of material properties, both lateral and vertical. Considerable improvement of volcano deformation models thus may be attained by taking into account spatial variations in the rheological properties (Currenti et al., 2011b; Masterlark et al., 2012; Pedersen et al., 2009). Geologic maps, tomographic images, and seismicity data provide information on

* Corresponding author at: Grupo de Volcanología de Barcelona (GVB-CSIC), SIMGEO (UB-CSIC), Institute of Earth Sciences Jaume Almera (CSIC), Lluís Solé Sabarís s/n, Barcelona 08028, Spain. Tel.: +34 93 409 54 10; fax: +34 93 411 00 12.

E-mail addresses: eronchin@ictja.csic.es, erikaronchin@gmail.com (E. Ronchin).

the distribution of material properties and stress regime, which often reveal a complex picture of the volcanic system.

This paper explores the capabilities of Abaqus software (Abaqus, 2009) in modeling a 3D volcanic system as a geometric pressure load embedded in an assembly of rheologic parts. We provide a strategy to use information on the distribution of material properties inferred from tomographic studies, among other geophysical and geological information, in order to create a 3D representation of geological bodies. The bulk of this analysis is devoted to creating parts using the Abaqus geometry definition functions: splines and solid lofts, implemented with Python scripts to automate execution of Abaqus commands. As a case-study, we apply our methodology to build a 3D model of the Rabaul Caldera, Papua New Guinea, in order to study the deformation that occurred between 11 August 1992 and 30 August 1993 in the area of Matupit Island (Saunders, 2001).

2. Method, 3D modeling strategies

The goal of this study is to provide a strategy to build a 3D geologic model using the Abaqus/CAE environment. Abaqus is a commercial software that uses Python commands during the model creation. The Python code provides access to Abaqus functions. We took advantage of this versatility developing some Python routines which significantly increased the flexibility of Abaqus functions and allowed for automated execution of hundreds of commands, as is necessary to produce complex 3D parts. To construct the 3D model, a CAE approach that allows simple creation and alteration of model geometries was used in combination with Python scripts, written to control the input points and the creation of splines and lofted volumes. For each recognized geologic region, an Abaqus part was first built with the help of the Python script and then modified by using boolean operations in the CAE environment during the assemblage of the model. Finally, all parts were merged into a single entity (Fig. 1), preserving the numerically welded boundaries of the individual parts.

The meshing procedure was preceded by the initial phase of constructing a suitably smooth solid geometric representation of the geologic body volumes deduced from geologic maps, earthquake locations, and tomographic images of Rabaul Caldera (Finlayson et al., 2003; Greene et al., 1986; Heming, 1974; Jones and Stewart, 1997; Mori and McKee, 1987; Saunders, 2001). Geologic bodies such as magma chambers have complex 3D shapes, so their solid representation assumes complex three-dimensional shapes that can be built by lofting the body through cross-sectional closed splines. In fact, considering a contour as a

continuous curve representing the intersection of a plane and the surface of an object, one technique for creating a solid volume is to imagine contours from different hypothetical slices and to loft a solid through these contours. The same technique can be used to construct a surface through many surface sections (Fuchs et al., 1977; Meyers et al., 1992). In our approach, to construct the primitive parts of the model as smooth 3D objects, we used discrete geo-referenced points obtained from tomographic images and geologic maps (Figs. 2 and 3a–d). Because the Abaqus solid-loft function uses a series of consecutive 2D cross sections bounded by closed splines to generate a volume, we needed to first identify some contours from the tomographic profiles and tomographic slices at different depth (e.g., magma chamber construction in Fig. 3c and d). Two-dimensional contouring involved fitting splines through a number of control points (Zhang et al., 2005) located along the 2D cross sections of the body. We first created contours and then sculpted the solid objects (magma chamber, caldera infill, etc.) by lofting them through their contours. The lofted object geometries were later modified and adjusted to the surrounding objects they were in contact with using partitions and boolean operations. The boolean operation makes use of primitive solid objects and utilizes the regularized boolean operators (union, difference, etc.) to combine the primitive objects into new solid objects. Finally, we assembled the entire model combining all the objects into one single part.

2.1. Identify control point coordinates and create an input file

The process of building a 3D geometry for an FEM consists of three main steps: (1) Choosing the control points, (2) Building the 3D parts, and (3) Assembling the parts to build the model. An additional step, meshing the resulting 3D construct, is discussed later.

Tomographic and geologic images were geo-referenced to the Universal Transverse Mercator (UTM) projection system through the open-source GIS software package QGIS (Quantum GIS Development Team, 2011). The UTM system has some advantages for Abaqus users. In this global coordinate system, a grid constructed on the Transverse Mercator projection of each longitude zone is used to locate points. The grid system is rectangular, decimal based, and has uniform units of measure that are amenable to Cartesian coordinate mathematics and suitable for the large scale domain of volcano deformation problems. This procedure enabled us to choose and obtain the spatial coordinates of strategic points which were later imported in Abaqus CAE and used as control points for the object spline contours (Fig. 3d). Points with UTM coordinates (X_i , Y_i , Z_i for East, North and up) are

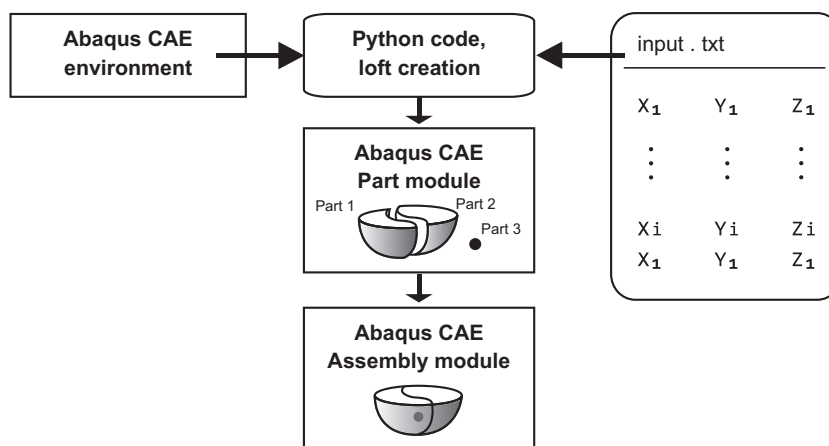


Fig. 1. Conceptual diagram of the model geometry construction.

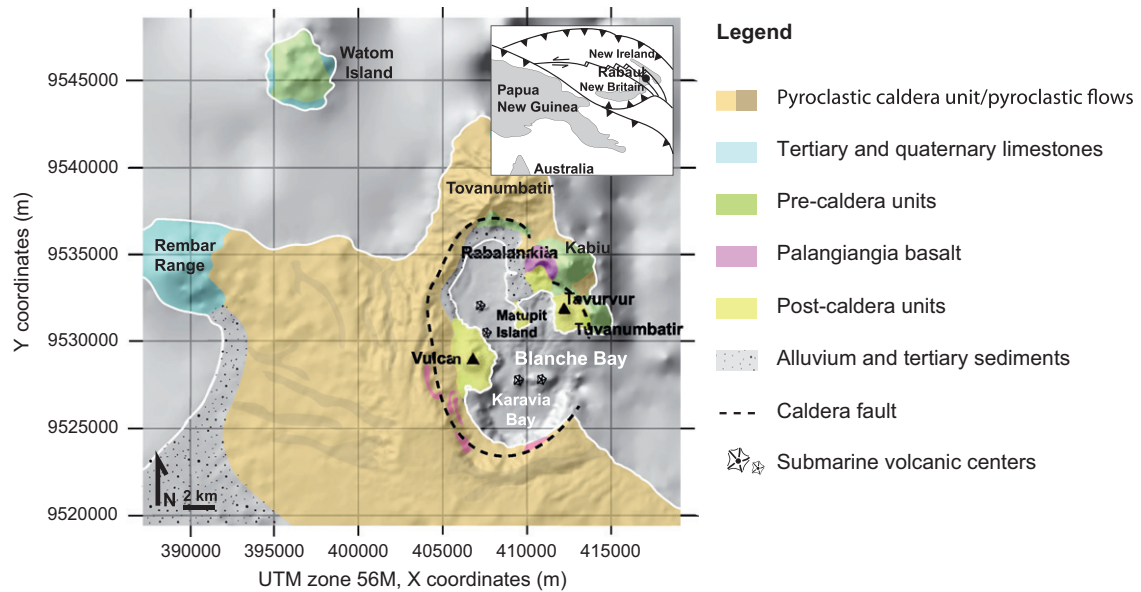


Fig. 2. Geology of the Rabaul Caldera (adapted from Heming (1974)).

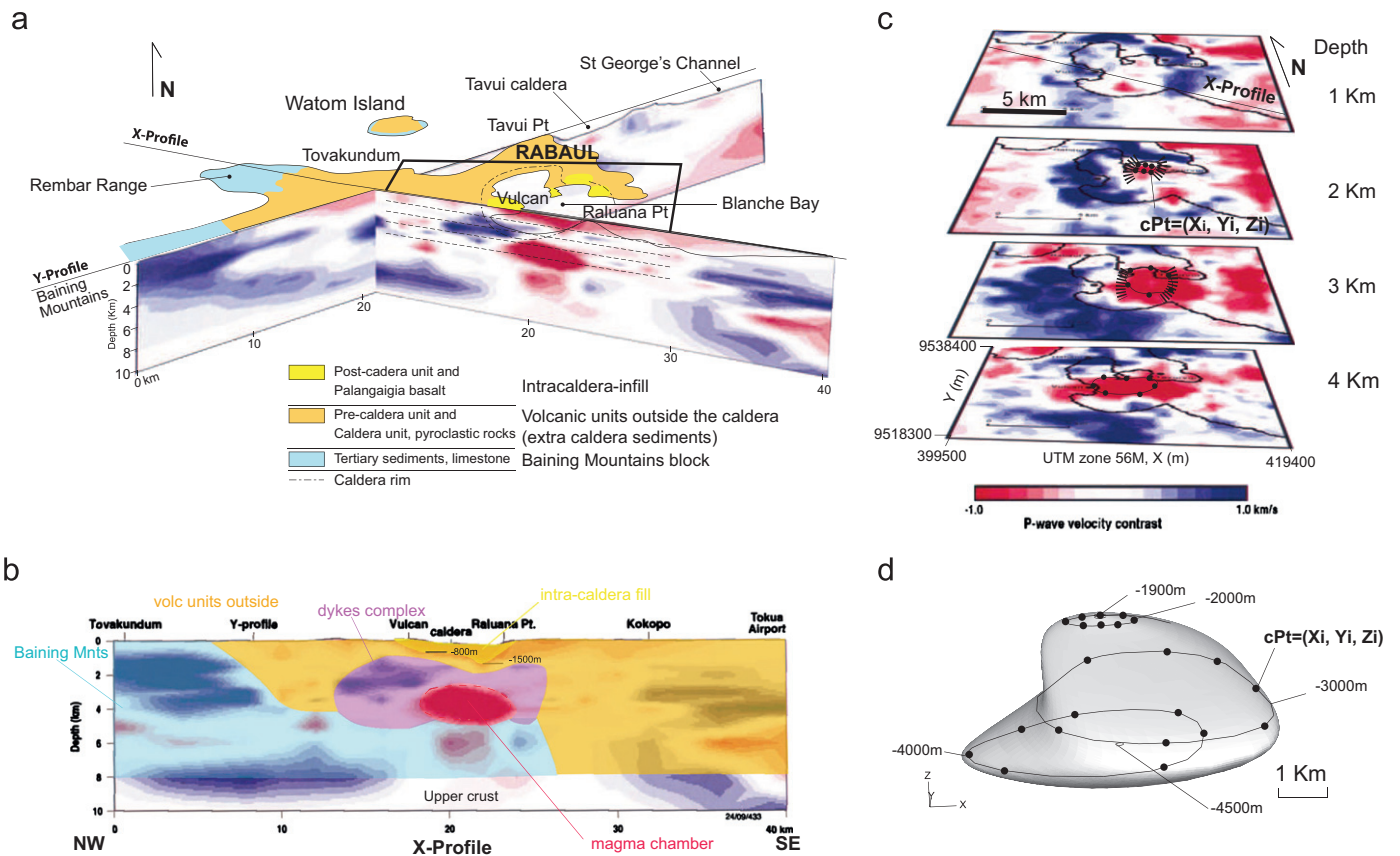


Fig. 3. Area study and parts construction. (a) Map of the geologic sub-domains on top of two tomographic profiles (adapted from Finlayson et al. (2003)). Footprint of the tomographic slices is shown (boxed area centered on Rabaul harbor). Dashed lines on X-Profile show the position of the slices at different depths. (b) Simplification of approximate geometry of the five geologic sub-domains from interpretation of Finlayson et al. (2003) tomography. (c) Slices at 1, 2, 3, and 4 km depths under the central Rabaul Caldera adapted from Finlayson et al. (2003). Solid lines are the contours used as reference for the magma chamber closed splines. Control points coordinates, $cPt=(X_i, Y_i, Z_i)$, are chosen along these contours. Dashed lines on the slices at 2 and 3 km represent the seismically active portions of the ring fault recognized by Jones and Stewart (1997), above 2 km and below 3 km, respectively. (d) Abaqus 3D solid part representing the magma chamber with splines and control points superimposed for clarity. The geometry of the magma body is achieved by lofting the solid through five horizontal closed sections at different depth (closed splines). Depth refers to sea level. Points in figure are the control points used to create the closed splines.

easily imported in the Abaqus cartesian space and ready to be used to build more evolved objects. In the UTM system, coordinate precision is readily understood; for our purposes,

coordinates are measured in meters and they translate directly to distances on the ground, allowing the user a rough preliminary control of the geometric model.

A good approach for the selection of spline control points (Fig. 3d) is to choose strategic points along the contour were to be represented by a spline (Fig. 3c) in Abaqus. Thus, the control point coordinates $cPt_i=(X_i, Y_i, Z_i)$ were obtained by manual selection of points along the chosen body contours (Fig. 3c) on a geo-referenced horizontal tomographic slice. For very precise 3D representation, this could be a drawback as it can lead to pronounced geometric discrepancies between the spline and the parent cross section perimeter (Young et al., 2008). However, this technique is suitable for geological purposes where the sections along which we select the control points are tomographic images characterized by resolution of kilometers (Finlayson et al., 2003) and smooth changes of V_p , which cannot resolve sharp boundaries between velocity anomalies. Abaqus CAE reads and imports the control point coordinates of closed contours from a text file through the first commands of the Python script (Appendix A). In the text file, the control point coordinates (X_i, Y_i, Z_i) have to be recorded in three columns. The points need to be specified in the order that the spline passes through them. Finally, the first and the last point have to be coincident in order to ensure the creation of a closed spline (Fig. 1).

2.2. Importing control points and creating part contours

All processes of importing points and generating closed splines were automated in a Python script (Appendix A). This script can be executed in Abaqus CAE. The script reads the input.txt file, imports the control point coordinates, recognizes the different depth values (Z_i) encountered in the file through the group index $I=2$ specified by the user, and calls the Abaqus function WireSpline, which generates a series of planar closed loops (one spline contour for each depth value encountered).

2.3. Assembling the model

Once we had all the parts needed (one for each geologic region), the model was assembled in the CAE Assembly module. With the use of boolean operations, two or more solids can be combined. Solid combination by boolean operators provides great flexibility to create a variety of shapes. First, all parts were reshaped using boolean operations in order to fit the neighbor

part surfaces. The advantage of using boolean operations is that they allow us to obtain new objects whose surfaces are precisely coincident with the adjoining parts, avoiding the formation of unwanted gaps in the model. The resulting parts were then stacked together from the upper crust parts to the mantle part forming a pile. The cavity for the magma chamber was created by subtracting the magma chamber solid from the pile, while the far field was shaped as a hemisphere by building a mold as a separate object and using it, through boolean operation cutting tools, to remove any exceeding volumes (outside of the wanted far field boundaries) of the piled layers.

3. A case-study: Rabaul Caldera, Papua New Guinea

We built the FEM to simulate the observed deformation of Rabaul Caldera as the result of pressurization of a magma chamber embedded in a heterogeneous elastic model domain. Expressed in index notation, the governing equations for the 3D elastic domain having spatially variable material properties are

$$\frac{\partial}{\partial x_i} \left[2G \left(\frac{\partial u_i}{\partial x_i} + \frac{\nu}{1-2\nu} \nabla \cdot u \right) \right] + \frac{\partial}{\partial x_j} \left[G \left(\frac{\partial u_i}{\partial x_j} + \frac{\partial u_j}{\partial x_i} \right) \right] = 0 \quad (1)$$

where u is displacement, G is the shear modulus, ν is Poisson's ratio. The subscripts i and j span orthogonal direction components $x, y,$ and $z,$ and $i \neq j.$

A complete description of an FEM includes the governing equations, the tessellated geometric domain, initial conditions, boundary conditions, and applied loads. The governing equations are given in Eq. (1). The 3D problem domain approximated a solid hemisphere with a diameter of 100 km centered on the caldera (Fig. 4). The outer surface of the hemisphere represented the far-field of the problem domain, and we assumed that it was far away enough from the caldera for displacements to vanish and to be specified as zero displacement. The magma chamber of the Rabaul system was simulated as a pressurized cavity. The loads applied to the system were both a pressure load along the wall of the embedded cavity and slip along a section of the ring fault.

The mesh used for this study has characteristic length of the element edges on the free surface of about 150 m above the magma reservoir, where a higher displacement gradient is expected, and gradually increasing characteristic lengths up to

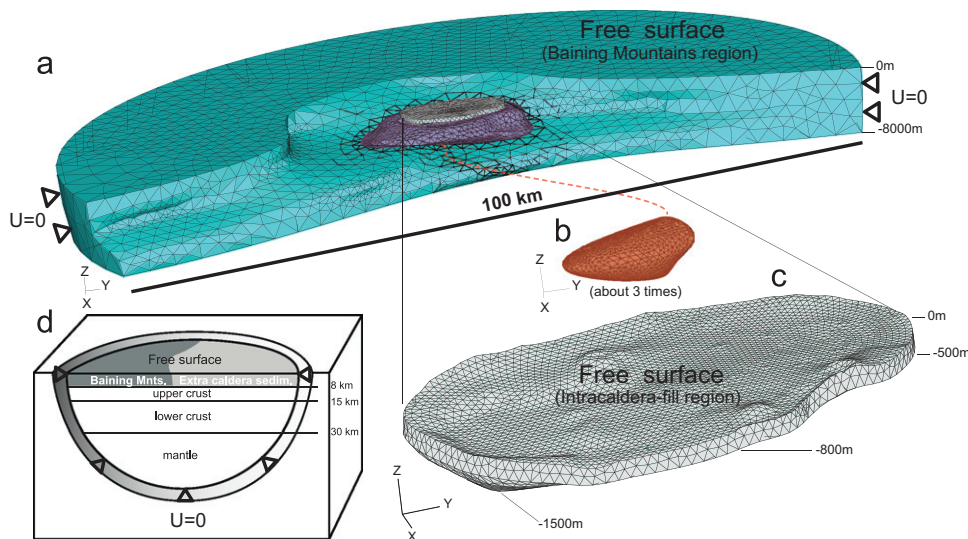


Fig. 4. FEM configuration. Parts of the upper eight km (a) Baining Mountains block (sky blue), dike complex block (violet), and intra-caldera fill block (light gray). Extra-caldera deposits block has been ignored to permit the visualization of inner parts. (b) Magma chamber magnified about three times for clarity. (c) Magnification of intra-caldera fill block. (d) General scheme of the model. (For interpretation of the references to color in this figure legend, the reader is referred to the web version of this article.)

about 3000 m near the far-field boundary where lower displacement gradients are expected. The element length near the magma chamber is about 300 m. Masterlark et al. (2012) validated a similar FEM configuration for volcano deformation.

3.1. Building the Rabaul Caldera geometry

Rabaul Caldera is a historically active collapse caldera system with an elliptic shape having major and minor axes of 14 and 9 km, respectively. Geologic relations document successive overlapping caldera forming events during the past few hundred thousand years accompanied by the eruption of dacitic ignimbrites, which largely filled the collapse depression (Heming, 1974, 1977; Heming and Carmichael, 1973; Nairn et al., 1995). These events resulted in a complex caldera shape and topography, and mechanical properties of caldera fill successions conspicuously different from the surrounding rocks. Since surface deformation is greatly influenced by material heterogeneities of the crust (Pedersen et al., 2009) and is very sensitive to the presence of weak materials within a caldera (Masterlark et al., 2012), we focused our attention on modeling the first eight kilometers (Figs. 3b and 4a, b and c). The choice of point coordinates, necessary to control the splines construction and used as input for the Python code to build the solids, was guided by the Finlayson et al. (2003) tomographic slices and the Heming (1974) geology previously geo-referenced through the QGIS-Grass functions (Fig. 2). The control points were input in UTM coordinates, the Y axis and X axis assumed, respectively, the North–South and West–East direction.

Based on the seismic tomography and geology, we chose to represent the domain with eight geologic bodies of different elastic properties (Table 1). These bodies were constructed as 3D deformable solid parts by using the lofting technique, partitions, and boolean operations in the Abaqus Assembly module. Based on the properties distribution derived from the tomographic sections and geological map, the upper part of the model (first 8 km of the upper crust) was subdivided into five solids: the Baining Mountains, the volcanic deposits external to the caldera, the infill deposits, the magma chamber, and the dike complex (Fig. 3b and Table 1). The remaining three regions were the mantle, the lower crust, and the upper crust (Fig. 4d). The transition between crust and mantle is located at a depth of 30 km; this assumption is justified by previous studies (Finlayson and Cull, 1973; Wiebenga, 1973).

At Rabaul Caldera, seismic hypocentral locations define an elliptical volume having horizontal major and minor axes of 10 and 5 km, respectively. This volume is interpreted as bounded by ring faults overlying a central region of low seismicity at depths below 2–4 km that is inferred to represent the present-day magma chamber (Mori et al., 1989; Lipman, 1997).

Due to the feasibility of making an arbitrary 3D shape in Abaqus, we have simulated the pressure source as a distributed load pressure in a single 3D reservoir having a complex shape with variable depth of the roof. The Rabaul reservoir cavity was inferred from tomographic slices (Fig. 3c). A region of magma accumulation under Blanche Bay was deduced from anomalously low P-velocity (V_p) distribution shown by the tomographic data (Finlayson et al., 2003). With the help of tomographic slices

Table 1
FEM configuration and parameters.

Parameter	Description	References
FEM domain extension	(UTM zone 56M) X_{\min} =Easting 3.6048e+05 m X_{\max} =Easting 4.6048e+05 m Y_{\min} =Northing 94.8075e+05 m Y_{\max} =Northing 95.8078e+05 m	
Center of FEM domain	4.1052e+05, 95.3091e+05 m UTM	
Analysis type	elastic	
Maximum FEM domain depth	50e+03 m	
FEM domain radius	50e+03 m	
Chamber volume	$32 \times 10^9 \text{ m}^3$	
FEM far field boundary conditions	Zero displacements	
Top of problem domain	Topographic relief	
Elements (1st order tetrahedra)	280,000	
Elastic formulas	$G = Vs^2 \cdot \rho$ and $E = 2G \cdot (1 + \nu)$, where G is the shear modulus and V_s was computed from V_p velocities, inferred from tomography (Finlayson et al., 2003)	
Intracaldera-fill	Density = 1900 kg/m ³ $V_s = 337 \text{ m/s}$ $E = 0.5 \times 10^9 \text{ Pa}$ $\nu = 0.15$	(McKee et al., 1984; Jaeger et al., 2007) from V_p velocities (Brocher, 2005 Eq. (6)). From elastic theory formulas (Wang, 2000)
Extra-caldera	Density = 2052 kg/m ³ $V_s = 882 \text{ m/s}$ $E = 4.08 \times 10^9 \text{ Pa}$ $\nu = 0.28$	(Brocher, 2005 Eq. (1), Rodríguez-Losada et al., 2009) from V_p velocities (Brocher, 2005 Eq. (6)) From elastic theory formulas. (Rodríguez-Losada et al., 2009)
Baining Mountains	Density = 2627 kg/m ³ $V_s = 2854 \text{ m/s}$ $E = 54.98 \times 10^9 \text{ Pa}$ $\nu = 0.28$	(Gardner et al., 1974) from V_p velocities (Brocher, 2005 Eq. (6)) From elastic theory formulas. (Christensen, 1996 Eq. (1))
Dikes complex	Density = 2936 kg/m ³ $V_s = 3322 \text{ m/s}$ $E = 85.53 \times 10^9 \text{ Pa}$ $\nu = 0.29$	(Christensen, 1996) from V_p velocities (Brocher, 2005 Eq. (8)) From elastic theory formulas, (Turcotte and Schubert, 2002; Carlson, 2001) (Christensen, 1996 Eq. (1))
Upper crust	$E = 37.5 \times 10^9 \text{ Pa}$ $\nu = 0.25$	Masterlark (2007) Masterlark (2007)
Lower crust	$E = 200.724 \times 10^9 \text{ Pa}$ $\nu = 0.29$	Turcotte and Schubert (2002) Masterlark (2007)
Mantle	$E = 174.59 \times 10^9 \text{ Pa}$ $\nu = 0.28$	Turcotte and Schubert (2002) Turcotte and Schubert (2002)

(Finlayson et al., 2003) and distribution of earthquake focuses (Mori and McKee, 1987; Jones and Stewart, 1997; Saunders, 2001) we inferred the size and shape of the magma chamber. The outward-dipping ring fault structure overlying the central region of low seismicity is outlined by the location of the earthquake focuses of the above mentioned studies. Jones and Stewart (1997) recognized two elliptical faults at different depths: an outer elliptical fault which embraces a smaller inner elliptical fault in its northern end (Fig. 3c). As faults cannot propagate in molten rocks, we assumed that the magma chamber should be enclosed into the ring fault structure with a narrower and shallower intrusion below the northern end of the outer ring fault, between Matupit Island and Turanganan. This ring fault complexity reflects the complex shape of the magma chamber and also defines the extension of the magma body. We outlined closed contours around the low velocity zone of the tomographic slices at 2, 3, and 4 km depth of Finlayson et al. (2003) tomography and picked some control points (cPt) (Fig. 3c). Then, we used the Python script (Appendix A) to import the control points and to generate a spline curve for each relevant contour of the magma chamber in CAE. Finally, we lofted a solid through the sections defined by the splines in CAE. In order to create the smooth solid part representing the magma chamber (Fig. 3d), the splines curves were sequentially lofted from the bottom (contour 4500 m below the sea level) to the uppermost spline. The modeled magma chamber had a volume of $32 \times 10^9 \text{ m}^3$, in agreement with the volume calculated by Finlayson et al. (2003) and had a roof with variable depth: 1900 m under Greet Harbour, in good agreement both with the depth of 1800 m previously estimated from leveling and gravity data (McKee et al., 1989) and with the depth of 2000 m estimated from tilt data (McKee et al., 1985), and 3000 m under Vulcan in agreement with tilt measurements (McKee et al., 1985) and with the low velocity zone shown in the X-profile of Finlayson et al. (2003) tomography. The magma chamber bottom reached its maximum depth of 4500 m centrally under Blanche Bay.

The sediment and rock units outside the caldera are prevalently non-welded tuff (Heming, 1974; Heming and Carmichael, 1973; Nairn et al., 1995). The geometry of this volume was mainly inferred from the geologic map (Heming, 1974) and tomographic sections (Finlayson et al., 2003) (Fig. 3a). The intra-caldera fill (Fig. 3b) is defined by a region of low velocity detected by the tomography X-Profile (Finlayson et al., 2003) in the area of Blanche Bay and Vulcan edifice, filling the caldera topographic depression and gradually deepening from -800 m in the North to up to about -1500 m in the South, below Karavia bay. Finlayson et al. (2003) imaged high velocity features around the magma chamber and under the rim of Rabaul Caldera that were interpreted to be mafic intrusive rock and that here are assumed to be a swarm of mafic dikes (Fig. 3b).

Another high V_p region occurs west of Rabaul Caldera, from the surface down to 5–6 km depth, and represents the Baining Mountains range (Finlayson et al., 2003), which is made up of tertiary volcanoclastic sequences, volcanic sediments, and limestones all intruded by leucogabbros, adamellites, and granites. This range can possibly extend as a slab interfingering with unconsolidated sediments under the Rabaul Caldera, making part of the caldera basement (Heming, 1974; Madsen and Lindley, 1994; Finlayson et al., 2003). In the proximity of Rabaul Caldera, the Baining Mountains are mainly represented by limestone, as can be deduced from the presence of Rembar Range limestone about 20 km west of the caldera (Heming, 1974; Nairn et al., 1995) and limestone about 20 km north-west of the caldera, in Watom island (Heming, 1974) (Fig. 2).

Elastic properties were calculated from the V_p distribution provided by the tomography (Finlayson et al., 2003) and are

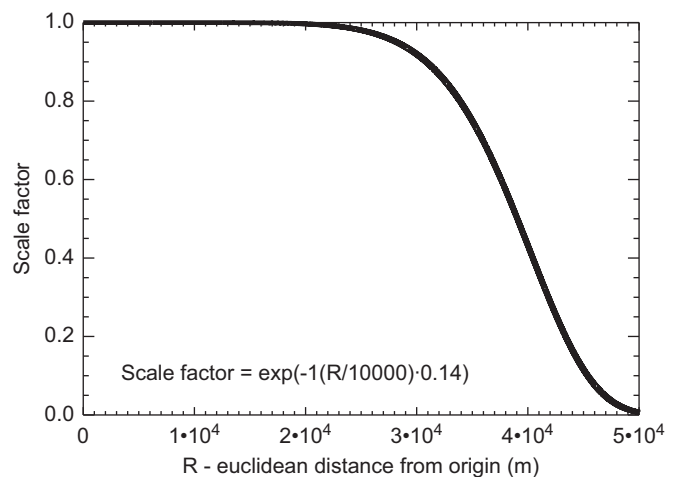


Fig. 5. Filter used to control distortion of the elements while applying the PMP to the free surface nodes in order to add the topography to the FEM. R is the distance of a free surface node from the center of the domain.

summarized in Table 1. Tomography and geology provided detailed information about the property distribution in an area of about 15 km radius centered around Rabaul Caldera. Outside of this perimeter, tomographic information was missing. We overcame this lack of information by extending the Baining Mountains and Extra-caldera sediments volumes to the domain boundaries.

Once the desired internal structure of the problem domain was built, the next step was to refine the geometry of the top of the problem domain in order to be more representative of the real land surface and sea floor. We used the Pinned Mesh Perturbation (PMP) method described by Masterlark et al. (2012) to generate the complex geometry of topographic and bathymetric relief of the stress-free surface. The terrain relief describing the geometry of the Earth's surface for both onshore and offshore regions of the model domain was compiled from three types of data having different resolution: the 90 m resolution SRTM data from the EROS-USGS website (EROS, 2011), the relatively coarse resolution (1-minute) gridded bathymetry data available from the GEBCO project website (GEBCO, 2011), and bathymetric data of Blanche Bay (RVO data). In order to avoid excessive element distortion during the perturbation of the mesh, we refined the mesh, reducing the size of the elements for areas having steep slopes, and we smoothed the displacements applied to the free surface nodes through a spatial filter (Fig. 5), which preserved the displacements in the central area of the free surface domain and reduced the applied displacements to zero along the border of the free surface. This way, the free surface was faithfully adapted to the topography in the area of interest (Rabaul Caldera) while avoiding large distortion due to the oceanic trench present in the areas far from the caldera center.

4. Deformation data modeling and results

We used the 3D FEM to simulate uplift at Rabaul Caldera comparable to leveling data published by Saunders (2001). First, in order to generate a deformation comparable to the observed one, an adequate change in pressure due to magma intrusion was derived from linear inversion of leveling data and applied to the magma chamber walls. We therefore assessed the calibration of two model parameters, the pressure change in the magma chamber, and the slip along a fault through linear inversion of the leveling data.

We modeled the displacements which occurred between August 1992 and August 1993 along the level line M (Saunders, 2001; Fig. 6 of this work) by inverting the data to first fit a source of pressure change and successively to fit the combination of a pressure change in the magma chamber and a normal dip slip fault along a segment of the ring fault.

Due to the traditional methods used to measure the caldera deformation, few level lines pass over the ring fault, so much detail of the complex deformation is missed. That means that only portions of the ring fault have any detailed data. For this reason we considered the portion of the ring fault that could greatly affect the deformation along the level line M that crosses the ring fault with closely spaced benchmarks (Fig. 6).

Deformations collected along level line T and those collected during July 1994 were not used because they are thought to be driven by the presence of deformation sources not taken into account in our model, such as the Talwat fault (Fig. 6) and a dilating fracture, respectively (Saunders, 2001).

Leveling data are of the First Order and Class I (Vanicek et al., 1980; Dzurisin, 2007). The accuracy estimates include both a length-dependent term to account for random surveying errors (Vanicek et al., 1980) and a time dependent term to account for vertical instability (Dzurisin et al., 2002; Wyatt, 1989). As the data of deformation are relative to the August 1992 survey taken as datum, the standard deviation of the height change is due to the contribution of the standard deviations of both surveys. Pelton

and Smith (1982) provided the formula to calculate the standard deviation of a height change measured by comparison of two leveling surveys:

$$\delta(\delta h) = \sqrt{\sigma_1(h)^2 + \sigma_2(h)^2} \quad (2)$$

where $\sigma_1(h)$ and $\sigma_2(h)$ are the standard deviation of height differences measured by the first and the second survey, respectively.

Computation of standard deviation of leveling measurements of level line M gives different values for each observed data, which means that every observation should not be treated equally during the inversion. Weighted least squares account for errors correlated to the measurement elevation by weighting the misfit using a matrix of data weights, \mathbf{W}_e , in order to give each data point its proper amount of influence over the parameter estimates. \mathbf{W}_e is a diagonal matrix containing the inverse of the standard deviation of leveling measurements (σ_i ; Menke, 1989). Thus, the \mathbf{W}_e matrix defines the relative contribution of each individual error to the total prediction error. The equation for the forward weighted model is

$$\mathbf{W}_e \mathbf{G} \mathbf{m} = \mathbf{W}_e \mathbf{d} \quad (3)$$

where \mathbf{G} is the model matrix, \mathbf{m} is the parameters vector, and \mathbf{d} is the column vector of leveling measurements. The linear least

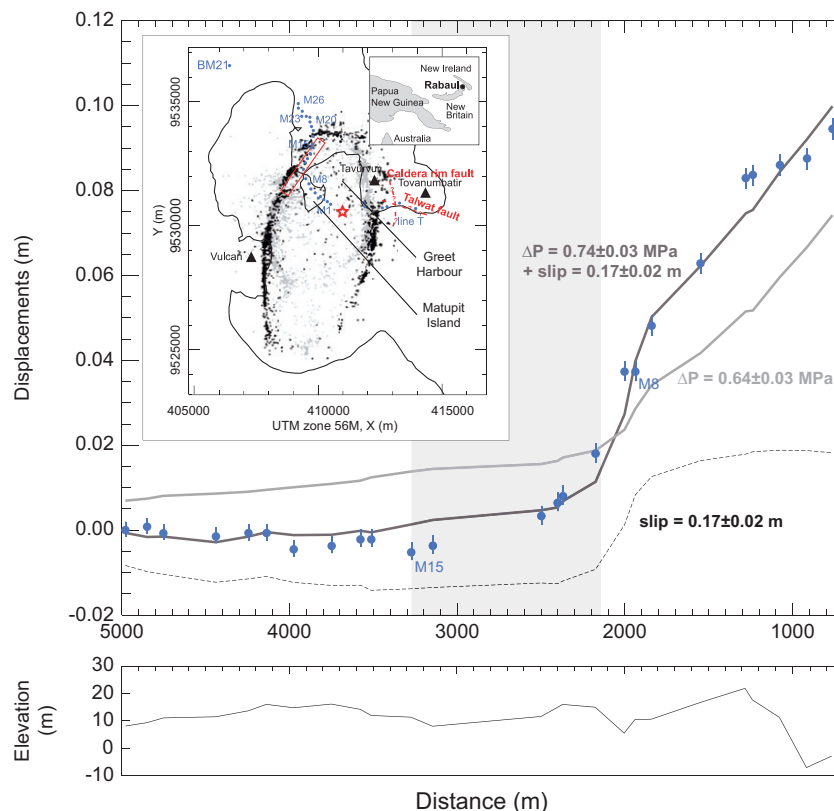


Fig. 6. Blue dots are the observed vertical displacements along level line M (Matupit, see inset), relative to datum point BM21, obtained comparing results for leveling survey of 11 August 1992 and 30 August 1993 (Saunders, 2001). Blue error bars are one standard deviation from length-dependent random surveying error (Vanicek et al., 1980) plus time dependent benchmark instability (Wyatt, 1989). Distance is measured radially from the projection of the shallower point of the modeled magma chamber on the surface. Displacements along level line M predicted by the FEM and due to the only change in pressure of 0.64 MPa in the magma chamber are shown in light gray; the predicted signal recovers 72% of the leveling signal. The dashed line and dark gray solid line represent the displacements at the same level line benchmarks generated respectively by slip of 0.17 m along the fault patch and by the combination of slip of 0.17 m along the fault and an increase of 0.74 MPa inside the magma chamber. The computed dark gray signal, resulting from the combination of the deformation sources, recovers 98% of the observed signal. Projection of the Okada fault patch on the surface (red rectangle) is shown in the upper left inset. Epicenters of earthquakes localized between 2 and 4 km (black) and between 2 and 0 km (light gray) are also plotted in the inset (modified from Saunders (2001)). (For interpretation of the references to color in this figure legend, the reader is referred to the web version of this article.)

Table 2
Parameters of the fault patch.

Dip slip dislocation (m)	0.17
Length (m)	2600
Width (m)	2600
Depth of Okada's origin-fault center (m)	2700 b.s.l.
Angle inclination (deg.)	82W
Angle strike (deg.)	216
Okada's origin in the center of the fault patch, UTM coordinates (m)	East 409,350 North 9,532,293

squares inverse solution for Eq. (3) is (Aster et al., 2005):

$$\mathbf{m}_{\text{est}} = [\mathbf{G}_w^T \mathbf{G}_w]^{-1} \mathbf{G}_w^T \mathbf{d}_w \quad (4)$$

where $\mathbf{G}_w = \mathbf{W}_e \mathbf{G}$ and $\mathbf{d}_w = \mathbf{W}_e \mathbf{d}$. This solution minimizes the sum of the weighted squared residuals, $\mathbf{e}^T \mathbf{W}_e \mathbf{e}$, where the residuals are $\mathbf{e} = [\mathbf{d} - \mathbf{u}_{\text{est}}]$ and $\mathbf{u}_{\text{est}} = \mathbf{G} \mathbf{m}_{\text{est}}$ is the vector of estimated vertical displacements.

Assuming only the change in pressure in the magma chamber as the deformation source, we built the model matrix \mathbf{G} using the FEM-generated impulse response functions (Masterlark, 2007), applying a unity pressure change (1 MPa) on the magma chamber walls. The parameter ΔP estimated by the weighted least squares linear inverse solution (Eq. (4)) is equal to 0.64 ± 0.03 MPa; the displacements predicted at the benchmarks by the FEM applying this pressure are shown in Fig. 6.

Assuming two complementary sources of surface deformation, the change in pressure ΔP in the magma chamber and the slip along a ring fault patch S (see Table 2 for fault patch parameters; Okada, 1992), the inversion analysis returns two parameter estimates: 0.74 ± 0.03 MPa and 0.17 ± 0.02 m, respectively (Fig. 6). The change in volume of the magma chamber related to the estimated overpressure is $4.0 \pm 0.16 \times 10^6$ m³.

5. Discussion and conclusions

We presented some strategies to integrate different types of information (geologic, tomographic, structural, and seismic data) in order to generate a complex 3D FEM of a volcanic system. Using contours, loft methods, and boolean operations in Abaqus CAE, integrated with the proposed Python script (Appendix A), we were able to take into account the spatial information of geologic bodies during the building process of 3D complex solids. The application of these strategies to the Rabaul Caldera case-study led to the construction of a new 3D FEM of the Rabaul system, but the same straightforward strategies can be applied to model any other volcanic system having the necessary constraining information for the internal structure (e.g. seismic tomography).

We compared the displacements predicted by the FEM to observed displacements, by applying a positive change in pressure of 0.64 MPa (inferred from the inversion of leveling data) to the walls of the magma chamber. Both FEM predictions and leveling data are strongly correlated with distance from the inflation center of Greet Harbour proposed by McKee et al. (1984, 1985). The FEM prediction recovers 72% of the leveling signal. The graph in Fig. 6 illustrates the strong discrepancy between the predicted and the observed signal, which we interpreted to be due to the effects of the slip along the portion of the ring fault. In order to verify this hypothesis and to better recover the observed deformation signal, as no discontinuities were simulated in the Rabaul Caldera FEM proposed here, in addition to the pressure source simulated by the FEM, we computed the contribution of the slip along the portion of the ring fault located across the leveling line M, using the Okada (1992) analytical model. Information about the shape of the fault patch and its

relative fault parameters were inferred from the distribution of ring seismicity in the area of leveling line M from Saunders (2001).

Earthquakes, generated as a response to overpressure in a shallow magma chamber, are focused along discontinuities (Troise et al., 1997) where shear slip takes place causing the upward motion of the inner collapsed area (De Natale and Pingue, 1993). The distribution of earthquakes thus gives important information about the dip and the geometry of the ring fault. The fault model parameters of the ring fault patch considered to be responsible for the deviation of 3D FEM predictions from the observed data, resumed in Table 2, are generally consistent with the distribution of hypocenters under level line M, which shows an active area between about 2000 and 4000 m depth (Jones and Stewart, 1997; Saunders, 2001) (Fig. 6).

By introducing a new parameter in the inverse analysis for slip, S, along the fault patch in addition to the change in pressure ΔP , we obtained new parameter estimates. The new predicted signal of the displacements obtained by summing the deformations predicted by the FEM and the Okada forward models recovers 98% of the observed signal (Fig. 6 dark gray), and thus well explains the deviation of the 3D FEM prediction from the observed signal as consequence of the strong influence of the slip along the ring fault patch.

Future studies using the proposed 3D FEM of Rabaul might focus on the understanding of the role property spatial variations and topography play in modifying the surface deformation. A further step in the improvement of the 3D Rabaul FEM can be done including the ring fault discontinuities in order to investigate the behavior of the ring fault and the interaction between the ring fault structure and the magma chamber.

Acknowledgments

This work is supported by JAE-PREDOC grant, CSIC (Consejo Superior de Investigaciones Científicas-Spanish National Research Council).

Appendix A. Supporting information

The Python script for the closed splines construction in a Abaqus 3D space is provided as supplementary data associated with this article.

Supplementary data associated with this article can be found in the online version at <http://dx.doi.org/10.1016/j.cageo.2012.09.025>.

References

- Abaqus, 2009. Version 6.9-EF. Dassault Systèmes Simulia Corp. Providence, RI <www.simulia.com>.
- Aster, R.C., Borchers, B., Thurber, C.H., 2005. Parameter Estimation and Inverse Problems. Elsevier Academic Press, San Diego, USA 301 pp.
- Bianchi, R., Coradini, A., Federico, C., Giberti, G., Sartoris, G., Scandone, R., 1984. Modelling of surface ground deformations in the Phlegraean Fields volcanic area, Italy. Bulletin of Volcanology 47 (2), 321–330.
- Brocher, T., 2005. Empirical relations between elastic wavespeeds and density in the Earth's crust. Bulletin of the Seismological Society of America 95 (6), 2081–2092.
- Carlson, R.L., 2001. The abundance of ultramafic rocks in Atlantic Ocean crust. Geophysical Journal International 144, 37–48, <http://dx.doi.org/10.1046/j.0956-540X.2000.01280.x>.
- Christensen, N.I., 1996. Poisson's ratio and crustal seismology. Journal of Geophysical Research 101, 3139–3156.
- Currenti, G., Napoli, R., Del Negro, C., 2011a. Toward a realistic deformation model of the 2008 magmatic intrusion at Etna from combined DInSAR and GPS observations. Earth and Planetary Science Letters 312 (1–2), 22–27.

- Currenti, G., Napoli, R., Di Stefano, A., Greco, F., Del Negro, C., 2011b. 3D integrated geophysical modeling for the 2008 magma intrusion at Etna: constraints on rheology and dike overpressure. *Physics of the Earth and Planetary Interiors* 185 (1–2), 44–52.
- De Natale, G., Pingue, F., 1993. Ground deformations in collapsed caldera structures. *Journal of Volcanology and Geothermal Research* 57, 19–38.
- Dieterich, J.H., Decker, R.W., 1975. Finite element modeling of surface deformation associated with volcanism. *Journal of Geophysical Research* 80 (29), 4094–4102, <http://dx.doi.org/10.1029/JB080i029p04094>.
- Dzurisin, D., 2007. *Volcano Deformation—Geodetic Monitoring Techniques*. Springer-Praxis Books in Geophysical Sciences, Berlin 441 pp.
- Dzurisin, D., Poland, M.P., Bürgmann, R., 2002. Steady subsidence of Medicine Lake volcano, Northern California, revealed by repeated leveling surveys. *Journal of Geophysical Research* 107 (B12), 2372–2388, <http://dx.doi.org/10.1029/2001JB000893>.
- EROS, 2011. Earth Resources Observation and Science (EROS) Center, US Geological Survey, <http://eros.usgs.gov/#/Find_Data> and <<http://earthexplorer.usgs.gov/>> (accessed December, 2011).
- Finlayson, D.M., Cull, J.P., 1973. Structural profiles in the New Britain/New Ireland region. *Australian Journal of Earth Sciences* 20 (1), 37–47, <http://dx.doi.org/10.1080/14400957308527893>.
- Finlayson, D.M., Gudmundsson, O., Itakarai, I., Nishimura, Y., Shimamu, H., 2003. Rabaul volcano, Papua New Guinea: seismic tomographic imaging of an active caldera. *Journal of Volcanology and Geothermal Research* 124, 153–171.
- Fuchs, H., Kedem, Z.M., Uselton, S.P., 1977. Optimal surface reconstruction from planar contours. *Communications of the ACM* 20 (10), 693–702.
- Gardner, G.H.F., Gardner, L.W., Gregory, A.R., 1974. Formation velocity and density—the diagnostic basics for stratigraphic traps. *Geophysics* 39, 770–780.
- GEBCO, 2011. General Bathymetric Chart of the Oceans, British Oceanographic Data Center. <http://www.gebco.net/data_and_products/gridded_bathymetry_data/> (accessed December, 2011).
- Geyer, A., Gottsmann, J., 2010. The influence of mechanical stiffness on caldera deformation and implications for the 1971–1984 Rabaul uplift (Papua New Guinea). *Tectonophysics* 483 (3–4), 399–412.
- Gottsmann, J., Folch, A., Rymel, H., 2006. Unrest at Campi Flegrei: a contribution to the magmatic versus hydrothermal debate from inverse and finite element modeling. *Journal of Geophysical Research* 111 (B07203), <http://dx.doi.org/10.1029/2005JB003745>.
- Greene, H.G., Tiffin, D.L., McKee, C.O., 1986. Structural deformation and sedimentation in an active caldera, Rabaul, Papua New Guinea. *Journal of Volcanology and Geothermal Research* 30, 327–356.
- Gudmundsson, A., Brenner, S.L., 2004. How mechanical layering affects local stresses, unrests, and eruptions of volcanoes. *Geophysical Research Letters* 31 (L16606), <http://dx.doi.org/10.1029/2004GL020083>.
- Heming, R.F., 1974. Geology and petrology of Rabaul Caldera, Papua New Guinea. *Geological Society of America Bulletin* 85, 1253–1264.
- Heming, R.F., 1977. Mineralogy and proposed P–T paths of basaltic lavas from Rabaul Caldera, Papua New Guinea. *Contributions to Mineralogy and Petrology* 61, 15–33.
- Heming, R.F., Carmichael, I.S.E., 1973. High-temperature pumice flows from the Rabaul Caldera Papua. *Contributions to Mineralogy and Petrology* 38, 1–20.
- Jaeger, J.C., Cook, N.G.W., Zimmerman, R.W., 2007. *Fundamentals of Rock Mechanics*, 4th ed. Blackwell Publishing, Malden, MA, USA 475 pp.
- Jones, R.H., Stewart, R.C., 1997. A method for determining significant structures in a cloud of earthquakes. *Journal of Geophysical Research* 94, 8245–8254.
- Lipman, P.W., 1997. Subsidence of ash-flow calderas: relation to caldera size and magma-chamber geometry. *Bulletin of Volcanology* 59, 198–218.
- Madsen, J.A., Lindley, I.D., 1994. Large-scale structures on Gazelle Peninsula, New Britain: implications for the evolution of the New Britain arc. *Australian Journal of Earth Sciences* 41, 561–569, <http://dx.doi.org/10.1080/08120099408728166>.
- Masterlark, T., 2007. Magma intrusion and deformation predictions: sensitivities to the Mogi assumptions. *Journal of Geophysical Research* 112, 17, <http://dx.doi.org/10.1029/2006JB004860>.
- Masterlark, T., Feigl, K.L., Haney, M., Stone, J., Thurber, C., Ronchin, E., 2012. Nonlinear estimation of geometric parameters in FEMs of volcano deformation: Integrating tomography models and geodetic data for Okmok volcano, Alaska. *Journal of Geophysical Research* 117, B02407, <http://dx.doi.org/10.1029/2011JB008811>.
- McKee, C., Mori, J., Talai, B., 1989. Microgravity changes and ground deformation at Rabaul Caldera, 1973–1985. In: Latter, J.H. (Ed.), *Volcanic Hazards: Assessment and Monitoring*. IAVCEI Proceedings in Volcanology, vol. 1. Springer, Berlin, pp. 399–428.
- McKee, C.O., Johnson, R.W., Lowenstein, P.L., Riley, S.J., Blong, R.J., De Saint Ours, P., Talai, B., 1985. Rabaul Caldera, Papua New Guinea: volcanic hazards, surveillance, and eruption contingency planning. *Journal of Volcanology and Geothermal Research* 23 (3–4), 195–237, [http://dx.doi.org/10.1016/0377-0273\(85\)90035-6](http://dx.doi.org/10.1016/0377-0273(85)90035-6).
- McKee, C.O., Lowenstein, P.L., De Saint Ours, P., Talai, B., Itikarai, I., 1984. Seismic and ground deformation crises at Rabaul Caldera: prelude to an eruption? *Bulletin of Volcanology* 47 (2), 397–411.
- Menke, W., 1989. *Geophysical Data Analysis: Discrete Inverse Theory*. International Geophysics Series, vol. 45. Academic, San Diego, California 289 pp.
- Meo, M., Tammaro, U., Capuano, P., 2007. Influence of topography on ground deformation at Mt. Vesuvius (Italy) by finite element modelling. *International Journal of Non-Linear Mechanics* 43 (3), 178–186, <http://dx.doi.org/10.1016/j.jnonlinmec.2007.12.005>.
- Meyers, D., Skinner, S., Sloan, K., 1992. Surfaces from contours. *ACM Transactions on Graphics* 11, 228–258, <http://dx.doi.org/10.1145/130881.131213>.
- Mori, J., McKee, C., 1987. Outward-dipping ring-fault structure at Rabaul Caldera as shown by earthquake locations. *Science (New York, NY)* 235, 193–195.
- Mori, J., McKee, C., Itikarai, I., Lowenstein, P.L., De Saint Ours, P., Talai, B., 1989. Earthquakes of the Rabaul seismo deformational crisis, September 1983 to July 1985: seismicity on a Caldera ring fault. *Volcanic hazards*. IAVCEI Proceedings in Volcanology vol. 1, pp. 429–462.
- Nairn, I.A., McKee, C.O., Talai, B., Wood, C.P., 1995. Geology and eruptive history of the Rabaul Caldera area, Papua New Guinea. *Journal of Volcanology and Geothermal Research* 69, 255–284.
- Okada, Y., 1992. Internal deformation due to shear and tensile faults in a halfspace. *Bulletin of the Seismological Society of America* 82, 1018–1040.
- Pedersen, R., Sigmundsson, F., Masterlark, T., 2009. Rheologic controls on inter-rifting deformation of the Northern Volcanic Zone, Iceland. *Earth and Planetary Science Letters* 281, 14–26, <http://dx.doi.org/10.1016/j.epsl.2009.02.003>.
- Pelton, J.R., Smith, R.B., 1982. Contemporary vertical surface displacements in Yellowstone National Park. *Journal of Geophysical Research* 87, 2745–2761.
- Pritchard, M.E., Simons, M., 2004. An InSAR-based survey of volcanic deformation in the Southern Andes. *Geophysical Research Letters* 31 (L15610), <http://dx.doi.org/10.1029/2004GL020545>.
- Quantum GIS Development Team, 2011. Quantum GIS Geographic Information System. Open Source Geospatial Foundation Project. <<http://qgis.osgeo.org>> (accessed December, 2011).
- Rodríguez-Losada, J.A., Hernández-Gutiérrez, L.E., Olalla, C., Perucho, A., Serrano, A., Eff-Darwich, A., 2009. Geomechanical parameters of intact rocks and rock masses from the Canary Islands: Implications on their flank stability. *Journal of Volcanology and Geothermal Research* 182 (1–2), 67–75.
- Saunders, S.J., 2001. The shallow plumbing system of Rabaul Caldera: a partially intruded ring fault? *Bulletin of Volcanology* 63, 406–420.
- Trasatti, E., Giunchi, C., Bonafede, M., 2003. Effects of topography and rheological layering on ground deformation in volcanic regions. *Journal of Volcanology and Geothermal Research* 122, 89–110.
- Trasatti, E., Giunchi, C., Piana Agostinetti, N., 2008. Numerical inversion of deformation caused by pressure sources: application to Mount Etna (Italy). *Geophysics Journal International* 172 (2), 873–884, <http://dx.doi.org/10.1111/j.1365-246X.2007.03677.x>.
- Troise, C., De Natale, G., Pingue, F., Zollo, A., 1997. A model for earthquake generation during unrest episodes at Campi Flegrei and Rabaul Calderas. *Geophysical Research Letters* 24, 1575–1578.
- Turcotte, D.L., Schubert, G.J., 2002. *Geodynamics: Applications of Continuum Physics to Geological Problems*, 2nd ed. Cambridge Univ. Press, New York 456 pp.
- Vanicek, P., Castle, R.O., Balazs, E.I., 1980. Geodetic leveling and its applications. *Reviews of Geophysics* 18, 505–524.
- Wang, H.F., 2000. *Theory of Linear Poroelasticity: With Applications to Geomechanics*. Princeton Univ. Press, Princeton, N. J. 287 pp.
- Wiebenga, W.A., 1973. Crustal structure of the New Britain–New Ireland region. In: Coleman, P.J. (Ed.), *The Western Pacific: Island Arcs, Marginal Seas, Geochemistry*. University of Western Australia Press, Nedlands, pp. 163–177.
- Wyatt, F.W., 1989. Displacement of surface monuments: vertical motion. *Journal of Geophysical Research* 94, 1655–1664.
- Yang, X.M., Davis, P.M., Dieterich, J.H., 1988. Deformation From Inflation of a dipping finite prolate spheroid in an elastic half-space as a model for volcanic stressing. *Journal of Geophysical Research* 93 (B5), 4249–4257, <http://dx.doi.org/10.1029/JB093iB05p04249>.
- Young, P.G., Beresford-West, T.B.H., Coward, S.R.L., Notarberardino, B., Walker, B., Abdul-Aziz, A., 2008. An efficient approach to converting three-dimensional image data into highly accurate computational models. *Philosophical Transactions of the Royal Society A* 366, 3155–3173, <http://dx.doi.org/10.1098/rsta.2008.0090>.
- Zhang, Z.Q., Zhou, J.X., Zhou, N., Wang, X.M., Zhang, L., 2005. Shape optimization using reproducing kernel particle method and an enriched genetic algorithm. *Computer Methods in Applied Mechanics and Engineering* 194, 4048–4070.